Optimizing Interface Conductivity in Electronics

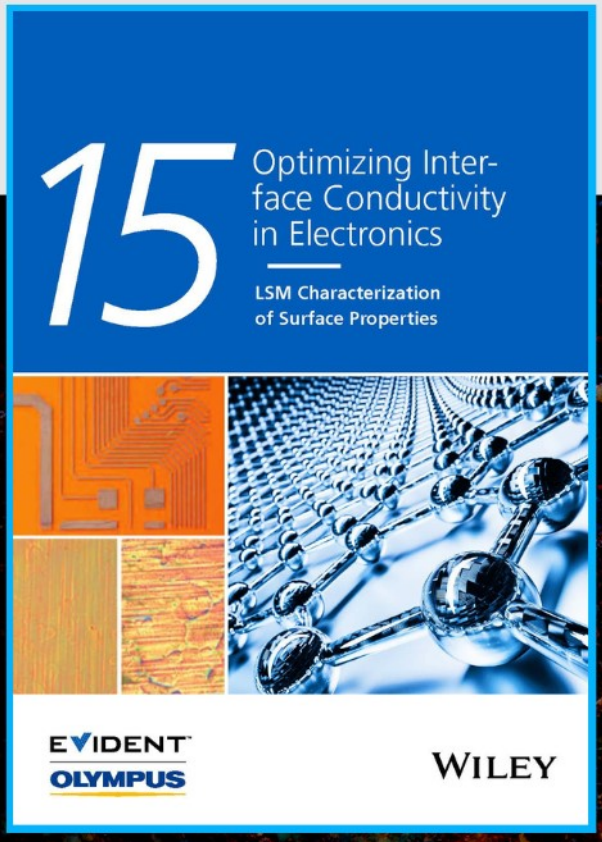

The latest eBook from Advanced Optical Metrology. Download for free.

Surface roughness is a key parameter for judging the performance of a given material's surface quality for its electronic application. A powerful tool to measure surface roughness is 3D laser scanning confocal microscopy (LSM), which will allow you to assess roughness and compare production and finishing methods, and improve these methods based on mathematical models.

Focus on creating high-conductivity electronic devices with minimal power loss using laser scanning microscopy is an effective tool to discern a variety of roughness parameters.

EVIDENT
OLYMPUS

WILEY

ADVANCED FUNCTIONAL MATERIALS
www.afm-journal.de

Robust Self-Catalytic Reactor for CO_2 Methanation Fabricated by Metal 3D Printing and Selective Electrochemical Dissolution

Hyo-Jin Kim, Kohsuke Mori, Takayoshi Nakano, and Hiromi Yamashita*

The methanation of CO_2 has been actively pursued as a practical approach to mitigating global climate change. However, the complexity of the catalyst development process has hindered the development of new catalysts for CO_2 methanation; as a result, few catalysts are commercially available. Herein, a multifunctional self-catalytic reactor (SCR) is prepared via metal 3D printing and selective electrochemical dissolution as a method to not only simplify the catalyst development process but also fabricate active catalysts for CO_2 methanation. The combination of metal 3D printing and selective electrochemical dissolution is demonstrated as a feasible method to prepare active catalysts for the methanation of CO_2 in a short time. In addition, the use of an electrochemical method enables the formation of galvanic cells on the SCR; these cells continuously generate active sites via self-dissolution during a simple refresh process, resulting in high reusability of the SCR. The proposed method represents a new facile technique to fabricate highly reusable catalysts that exhibit superior performance for CO_2 methanation, and the results provide a guideline for preparing metal 3D-printed catalysts that will satisfy industrial demand.

1. Introduction

CO_2 methanation, the so-called Sabatier reaction ($CO_2 + 4H_2 \rightarrow CH_4 + 2H_2O$, $\Delta H = -165.0$ kJ mol^{-1}), is of great interest not only as a method to store energy with high density but also as a promising energy source in near-future energy scenarios.[1,2] This reaction also has the potential to reduce atmospheric CO_2 levels by utilizing CO_2 as an inexpensive, nontoxic, and abundant C1 feedstock and could ultimately provide a carbon-neutral cycle. Because the methanation of highly stable CO_2 requires massive energy input, a reliable catalyst is generally used to lower the activation energy and accelerate the conversion.[3,4] In particular, heterogeneous catalysts that exhibit high stability and efficiency are considered suitable for CO_2 methanation. Topics related to these catalysts, including alloying methods, nanoparticle properties, single-atom shapes, and various supports, have therefore been actively investigated in recent years.[5–7]

Despite extensive effort having been devoted to developing catalysts for the methanation of CO_2, most of the reported catalysts are not suitable for use beyond the laboratory scale; in addition, only a few catalysts are commercially available because of the complexity of the catalyst development process.[3,8,9] The traditional process consists of four logical steps: catalyst design and performance testing; solidification; a pilot test with a scale-up; and finally industrial application.[9] The initial two processes depend on the intrinsic properties of the catalysts themselves, and the last two sequential steps are related to the hydrodynamic properties of reactors as well as their performance.[10,11] These observations indicate that the properties of the catalysts and reactors must be considered simultaneously when developing a new catalyst. Unfortunately, catalysts and reactors for CO_2 methanation have been researched in different directions, resulting in conflicting concepts between them, which have hindered the development of new catalysts.[12] Hence, new catalytic systems that integrate complex processes are needed for the development of new catalysts not only for CO_2 methanation but also other reactions.

Recently, the use of metal 3D-printing methods such as selective laser melting (SLM), selective laser sintering, and direct metal printing in the catalyst field has been expanding to simplify the development process and provide a wide range of

H.-J. Kim, K. Mori, T. Nakano, H. Yamashita
Division of Materials and Manufacturing Science
Graduate School of Engineering
Osaka University
2-1 Yamadaoka, Suita, Osaka 565-0871, Japan
E-mail: mori@mat.eng.osaka-u.ac.jp
K. Mori, T. Nakano
Anisotropic Design & Additive Manufacturing Research Center
Osaka University
2-1, Yamadaoka, Suita, Osaka 565-0871, Japan
K. Mori, H. Yamashita
Innovative Catalysis Science Division
Institute for Open and Transdisciplinary Research Initiatives (ICS-OTRI)
Osaka University
Suita, Osaka 565-0871, Japan

The ORCID identification number(s) for the author(s) of this article can be found under https://doi.org/10.1002/adfm.202303994

DOI: 10.1002/adfm.202303994

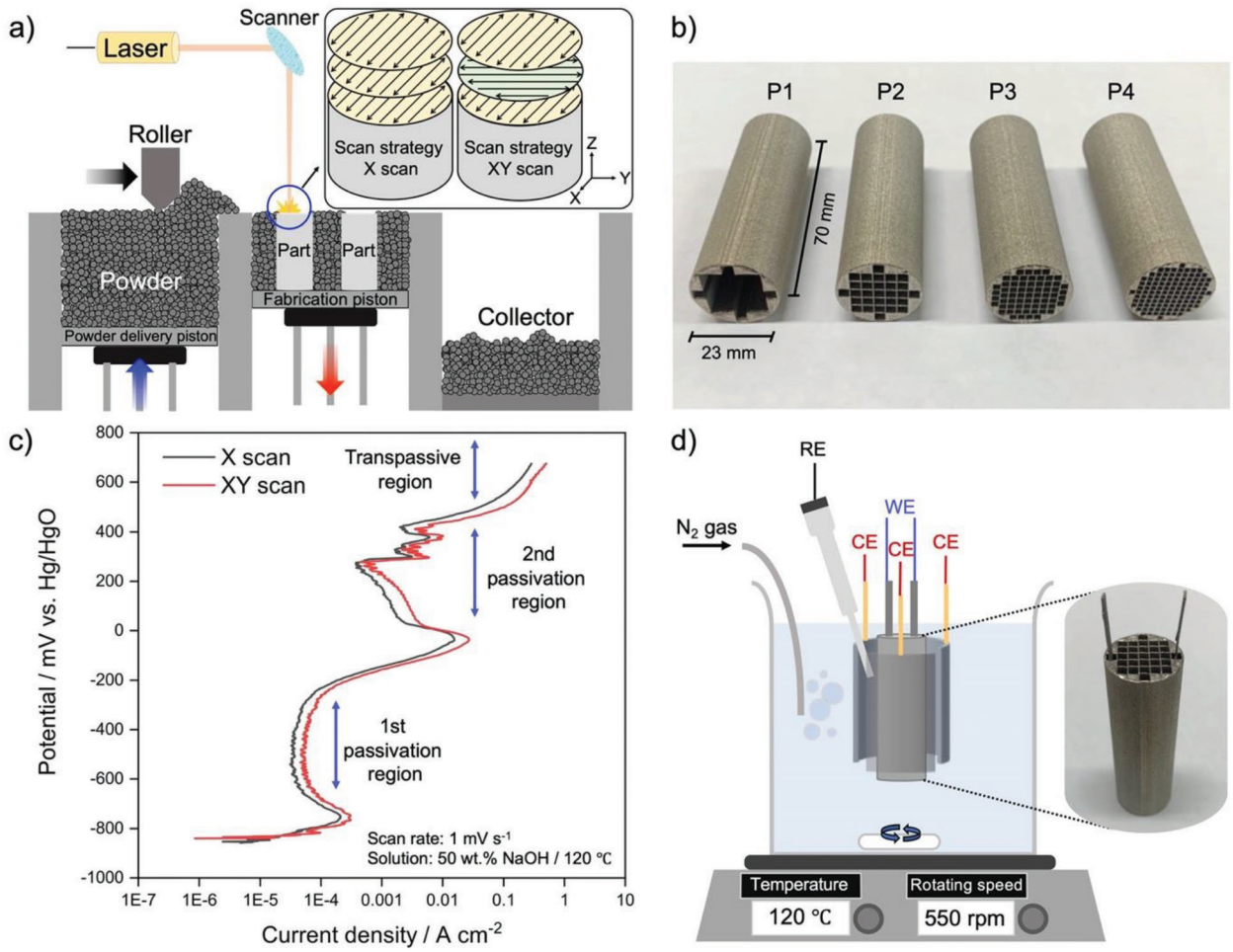

Figure 1. a) Schematic of selective laser melting process with two different scan strategies. b) Photograph of as-printed SCR with four types of patterns. c) Anodic polarization curves for *X*- and *XY*-scan SCRs immersed in 50 wt% NaOH at 120 °C. d) Schematic of selective electrochemical dissolution process, where RE, WE, and CE represent the reference electrode, working electrode, and counter electrode, respectively.

functions to catalysts.[13–15] The metal 3D-printed reactor known as a "self-catalytic reactor" (SCR) simultaneously functions as both a catalyst and a reactor, feasibly integrating performance and hydrodynamic properties simultaneously.[15] Moreover, the high geometric flexibility of metal 3D printing facilitates optimization of the hydrodynamic behavior of the reactor and provides high thermoelectrical conductivity.[16,17]

CO_2 methanation is an exothermic reaction, and traditional catalysts suffer from the formation of hotspots, which lead to irreversible deactivation of the catalyst via sintering.[18,19] On this basis, the application of the integrated functions of SCRs for CO_2 methanation can overcome the existing obstacles and minimize the labor and time required for catalyst development, thereby accelerating the development of new catalysts for the methanation of CO_2. Nevertheless, SCR research is in its early stages; knowledge related to the fabrication and, especially, the surface treatments of SCR is lacking.

In the present work, we developed a cylindrical-shaped Ni-based SCR by SLM using Hastelloy X powder as a starting material. Selective electrochemical dissolution of the SCR successfully transformed the original inert surface, which consisted of a Cr- and Fe-based passivation layer, into a Ni-enriched surface that is active as a robust catalyst for CO_2 methanation. Notably, we demonstrate for the first time an SCR that enables a continuous increase in catalytic activity through a simple refreshment process driven by a self-dissolution mechanism. Other important factors, such as the effect of different crystal textures induced by different scan strategies on the selective electrochemical dissolution process and the relationship between the geometric structure of the SCR and its thermal properties, are also investigated.

2. Result and Discussion

2.1. Selective Electrochemical Dissolution for Different Applied Potentials

The SCRs were fabricated by laser powder bed diffusion (LPBD) using Ni-21Cr-18Fe-8Mo at% powder as a starting material by two different scan strategies, *X* and *XY* scan (**Figure 1**a). The cylindrical-shaped structures 23 mm in diameter × 70 mm in length and with four different cell densities (P1, P2, P3, and P4) are shown in Figure 1b. There is no lattice in the P1. To increase

the internal surface area, the number of blocks was increased from 29 to 113 for P2 to P4, whereas the thickness of the pillars was fixed at 0.2 mm (Figure S2, Supporting Information). The as-printed Ni-SCR was prepared without any cracks; however, its surface was covered mostly with 54.5 at% Cr and 29.9 at% Fe, which means that the as-printed specimen could not be used as an active SCR for CO_2 methanation (Figures S3 and S4, Supporting Information).[20]

Selective electrochemical dissolution is a promising method to transform a metal surface into a surface enriched with certain metal components within a short time.[21] To transform the inert as-printed Ni-SCR into an active catalyst for CO_2 methanation by selective electrochemical dissolution, a suitable potential should be applied because the surface properties are dramatically influenced by the variation of the surface electronic state and stable species.[22] Hence, the anodic potentiodynamic polarization curve of Ni-SCR was conducted in 50 wt% NaOH at 120 °C to verify the dissolution behavior and elucidate the variation of the surface in response to the potential shift (Figure 1c). The curve shows two passivation regions with different current densities, implying that the Ni-SCR surface properties varied substantially with the applied potential. Therefore, we selected five different potentials between two passivation regions to investigate the effect of the applied potential on the surface properties of the Ni-SCR and the CO_2 methanation activity. The differences in dissolution properties between the *X*-scan and *XY*-scan SCRs are detailed in the next section.

Figure 1d illustrates the selective electrochemical dissolution process. A metal 3D-printed clip printed under the same conditions as the Ni-SCR was attached to the Ni-SCR as an electrical connection and to prevent the formation of a mixed potential between the Ni-SCR and the connection. The Ni-SCR was subsequently immersed in 50 wt% NaOH at 120 °C and surrounded by Pt counter electrodes used to generate a uniform electric field. The selective electrochemical dissolution process was carried out for 3 h at each potential.

The Ni-SCR after electrochemical treatment at different applied potentials was evaluated by scanning electron microscopy (SEM)/EDS and X-ray diffraction (XRD) analysis (**Figure 2**a–c). Cr and Fe remained on the surface even after a −300 $mV_{Hg/HgO}$ potential was applied, although a peak attributable to $Ni(OH)_2$ was observed in the XRD pattern, indicating that the $Ni(OH)_2$ phase randomly covered the Ni-SCR surface. When the applied potential was increased to 50 $mV_{Hg/HgO}$, the surface enrichment with $Ni(OH)_2$ increased, which we attributed to the stability of $Ni(OH)_2$ formed in a hot alkaline solution by direct transformation ($Ni^0 + 2OH^- \rightarrow Ni(OH)_2$) or by the dissolution–reprecipitation mechanism ($Ni^0 \rightarrow Ni^{2+} + 2OH^- \rightarrow Ni(OH)_2$).[21,23] By contrast, Cr, Fe, and Mo species were thermodynamically unstable and selectively dissolved as CrO_4^{2-}, $Fe(OH)_4^-$, and MoO_4^{2-}, respectively.[24–26] SEM images subsequently acquired for Ni-SCR specimens subjected to applied potentials between 200 and 360 $mV_{Hg/HgO}$ showed that the surface $Ni(OH)_2$ transformed into agglomerated species. The change in morphology and disappearance of the $Ni(OH)_2$ peak in the XRD pattern implied that $Ni(OH)_2$ was transformed into Ni^{3+} species (e.g., $NiO_x(OH)_{2-2x}$ and NiOOH) because of the increase of the oxidation degree with increasing polarization.[22] The decrease in current density at applied potentials between 50 and 300 $mV_{Hg/HgO}$ in Figure 1c also indicates that the Ni^{3+} species in this region tended to form a more compact film than $Ni(OH)_2$, preventing the selective dissolution of the SCR and resulting in a decrease in the Ni content observed by EDS analysis. The pulsation of the current densities in the 300–500 $mV_{Hg/HgO}$ range is attributed to initiation of the oxygen evolution reaction (OER, $O_2 + H_2O + 4e^- \rightleftharpoons 4OH^-$, pH 14, 0.299 $mV_{Hg/HgO}$) and the formation of β/γ-NiOOH.[23] However, when the applied potential was increased to 630 $mV_{Hg/HgO}$, the current density started to actively increase and a massive OER on the SCR during electrochemical treatment was observed, along with transpassive dissolution of surface species.[27]

The near-surface region was also investigated by XPS measurements (Figure 2d and Figures S4 and S5, Supporting Information). Before the electrochemical treatment, most of the surface of the as-printed Ni-SCR consisted of a mixture of Cr and Fe oxide species, with 11.8 at% Ni species (Figure S4, Supporting Information). Similarly, when a −300 $mV_{Hg/HgO}$ potential was applied, the Ni content increased to 33.3 at% and Cr was the dominant species (44.4 at%). In contrast, when a 50 $mV_{Hg/HgO}$ potential was applied, the Ni content reached 94.9 at%, representing a nine-fold increase in the amount of enriched Ni on the surface region. The Ni 2p peak and low value of the ratio between metal bonded to lattice oxygen (M–O) and metal bonded to a hydroxyl group (M–OH), as determined from the O 1s peak in the XPS spectrum of the specimen treated at 50 $mV_{Hg/HgO}$, indicate that most of Ni in this specimen likely existed as $Ni(OH)_2$ (Figure S6, Supporting Information).[28] Further increase of applied potential to 200 and 360 $mV_{Hg/HgO}$ resulted in an increase of the metal oxide M–O/M–OH ratio from 0.23 to 0.56, which indicated the transformation of $Ni(OH)_2$ into $NiO_x(OH)_{2-2x}$ and γ-NiOOH, consistent with the SEM/EDS results. When the potential was increased to 630 mV $mV_{Hg/HgO}$, the Ni content and M–O/M–OH ratio decreased and the Cr content increased, indicating that the Ni SCR raw substrate was subjected to be exposed by transpassive dissolution. The overall process of selective electrochemical dissolution was described in Figure S7, Supporting Information.

2.2. Selective Electrochemical Dissolution with Different Scan Strategies

In the metal 3D-printing process, different scan strategies generate distinct crystal textures because of different thermal gradients during the build-up.[29,30] The crystal-texture properties, such as the grain size, grain boundaries (GBs), and dislocations are deeply correlated with the dissolution of the metal; therefore, the application of an appropriate scan strategy is a critical factor for optimizing the selective electrochemical dissolution process.[31] In Figure 1c, the *XY*-scan SCR shows a higher current density than the *X*-scan SCR, implying a difference in dissolution behavior between the *X*- and *XY*-scan Ni-SCRs, which is attributed to the dissimilarity of their crystal textures. Similarly, the selective electrochemical dissolution experiments at 50 $mV_{Hg/HgO}$ also indicate differences between the *X*- and *XY*-scan Ni-SCRs (**Figure 3**a). These results show that the current density for both Ni-SCRs tended to be high at the initial stage before decreasing to a stable value, which is attributed to rapid nucleation and growth

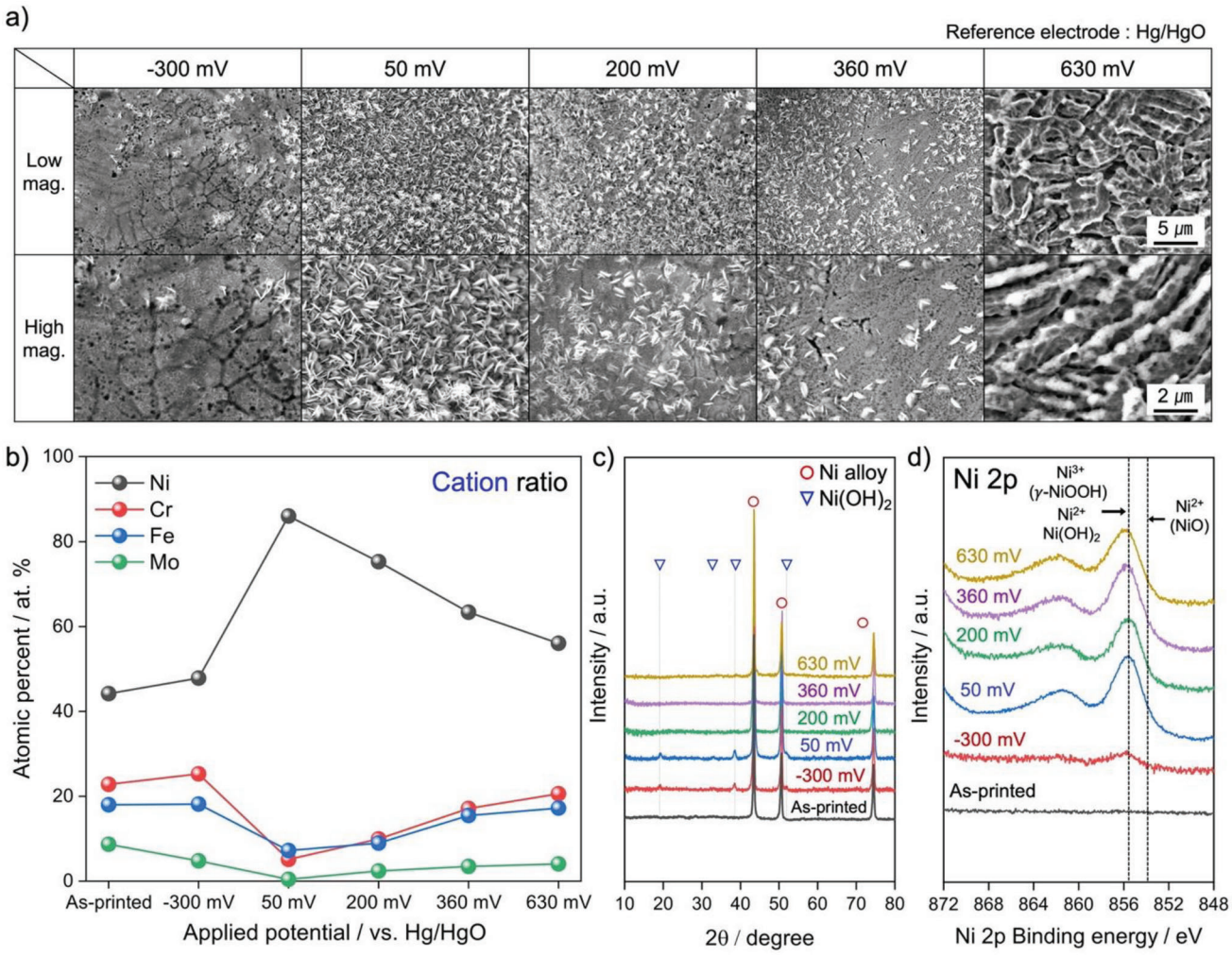

Figure 2. a) Low- and high-magnification SEM images of SCRs after selective dissolution at different applied potentials. b) EDS results for SCRs after selective dissolution at different applied potentials. c) XRD profiles of SCRs after selective dissolution at different applied potentials. d) Ni 2p XPS spectra of SCRs after selective dissolution at different applied potentials.

of a passivation film (i.e., a $Ni(OH)_2$ film) on their surface during a 3 h electrochemical treatment.[32] In contrast, the initial and steady-state current density differed substantially between the *X*- and *XY*-scan Ni-SCRs, implying a difference in the quality of the passivation film on each SCR.[33] Therefore, we transformed Figure 3a into a double-log plot to estimate the compactness of the surface $Ni(OH)_2$ film (Figure 3b). The compactness of the surface $Ni(OH)_2$ film can be evaluated by a double-log plot using the Macdonald model: $\log i = \log A - n\log t$, where i is the current density, t is the treatment time, and A and n are constants. The n-value represents the compactness of the passivation film, where $n \approx -1$ indicates a compact film.[33] In Figure 3b, the n-values for the *X*- and *XY*-scan Ni-SCRs are −0.26 and −0.17 in the initial stage and eventually reach −0.98 and −0.93, respectively. In addition, the *X*-scan Ni-SCR shows a higher current density at initial stage and reverse with the *XY*-scan Ni-SCR after ≈600 s, demonstrating that the surface $Ni(OH)_2$ film on the *X*-scan Ni-SCR was formed more rapidly and with greater compactness than the film on the *XY*-scan Ni-SCR.

Electrochemical impedance spectroscopy results measured in 50 wt% NaOH also show an obvious difference in the total resistance (R_{tot}) between the *X*-scan (1960.6 Ω cm^2) and *XY*-scan (387.4 Ω cm^2) Ni-SCRs, indicating the formation of a more compact surface $Ni(OH)_2$ film on the *X*-scan Ni-SCR (Figure 3c and Table S2, Supporting Information). Due to the deteriorated quality of passivation film on *XY* scan Ni-SCR, a comparison of the cross-sectional SEM image illustrated that *XY* scan Ni-SCR contained thick $Ni(OH)_2$ layer formed by continuous selective dissolution (Figure 3d). Characterization of the electrolytes by inductively coupled plasma atomic emission spectroscopy after the selective electrochemical dissolution at 50 $mV_{Hg/HgO}$ also suggested that the *XY*-scan Ni-SCR showed superior selective electrochemical dissolution (Table S3, Supporting Information).

The quality and formation of the surface $Ni(OH)_2$ film were extensively influenced by the crystallographic texture properties. As analyzed by electron backscatter diffraction (EBSD), both Ni-SCRs showed clearly different polycrystalline microstructures depending on the scan strategy (Figure 3e). The *X*-scan strategy

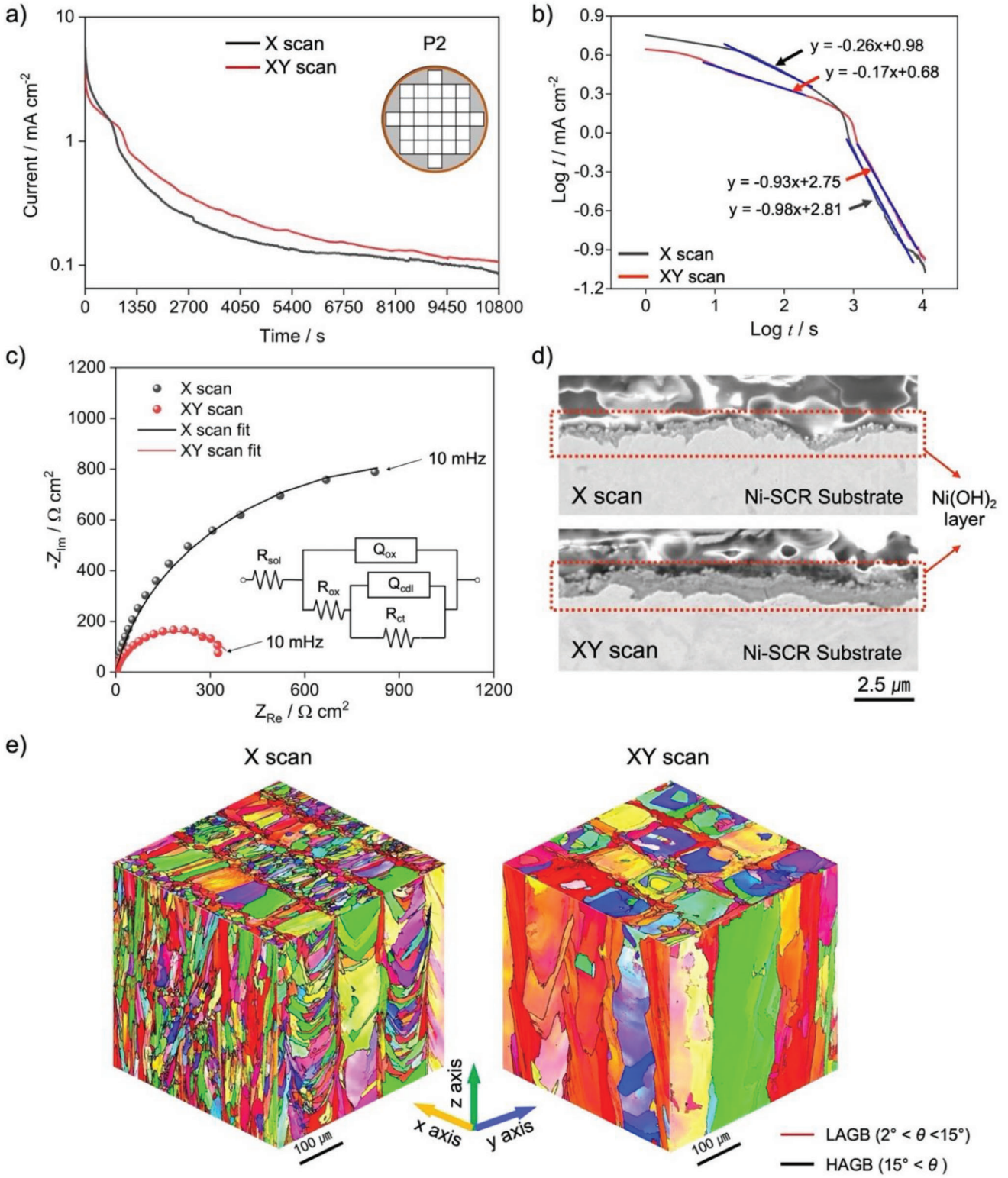

Figure 3. a) Plot of current density versus time curves of the *X*- and *XY*-scan SCR-P2 specimens under applied potential of 50 $mV_{Hg/HgO}$. b) Transient current density versus time plotted on double-log scales. c) Nyquist spectra of *X*- and *XY*-scan SCR-P2 specimens after selective electrochemical dissolution at 50 $mV_{Hg/HgO}$. d) Cross-sectional view of *X*- and *XY*-scan SCR-P2 specimens after selective electrochemical dissolution at 50 $mV_{Hg/HgO}$. e) 3D visualization of EBSD inverse pole figure images of *X*- and *XY*-scan SCRs with low-angle and high-angle grain boundaries (LAGB and HAGB, respectively).

only scanned along the planes, whereas the *XY* strategy not only scanned along the planes but also across the planes, resulting in a divergence in the crystal texture.[34] The crystal texture for the *X*-scan Ni-SCR showed 60–70°-tilted columnar grains along the scan direction in the *XZ* plane and semicircular-shaped grains with some single-crystal-like structures in the *YZ* plane. On the *XY* plane, there was a long columnar grain shape along the melt pool wall. However, in the case of *XY*-scan Ni-SCR, the scan direction alternated along the *XZ* and *YZ* planes, creating a texture similar to a mixture of 60–70°-tilted and 90°-vertical-direction grains. Moreover, the alternating scan caused remelting of small equiaxed grains on the melt-pool boundary and thereby formed a checkboard shape on the *XY* plane.[29] Interestingly, the average grain size on each plane of the *X*-scan Ni-SCR was much finer than that on each plane of the *XY*-scan Ni-SCR (Table S4, Supporting Information).[35,36] Specifically, the average grain sizes in the *XY* plane were 7.61 µm (*X* scan) and 13.26 µm (*XY* scan), the average grain sizes in the *XZ* plane were 11.42 µm (*X* scan) and 16.97 µm (*XY* scan), and the average grain sizes in the *YZ* plane were 11.30 µm (*X* scan) and 15.65 µm (*XY* scan). Grain size is a critical factor that affects the quality of surface-exposed films since an increase in the density of reactive GBs critically affects the formation of nucleation sites on a surface-exposed film by enabling the formation of a dense microgalvanic cell.[37] Therefore, the fine grain size in the *X*-scan Ni-SCR contributed to the rapid formation of a compact surface $Ni(OH)_2$ film with a large number of nucleation sites, coinciding with the high current density at the initial stage and steeply decrease on the electrochemical treatment (Figure 3b). In addition, not only GBs but also the high dislocation densities are known to function as nucleation sites for the surface $Ni(OH)_2$ film.[38] Hence, we also collected geometrically necessary dislocation (GND) density images, which represent the density of dislocations (Figure S8, Supporting Information). The results show that the *X*-scan Ni-SCR exhibited 1.46-, 1.33-, and 1.48-fold greater density on its *XY*, *XZ*, and *YZ* planes, respectively, compared with the *XY*-scan Ni-SCR. Overall, the finer grain size in conjunction with a high dislocation density in the *X*-scan Ni-SCR promoted the formation of a more uniform and thicker $Ni(OH)_2$ layer on the Ni-SCR surface. However, although the GB angle also affected the surface $Ni(OH)_2$ film, the non-uniformity of the ratio of the number of low-angle grain boundaries to the number of high-angle grain boundaries between *X*- and *XY*-scan Ni-SCR implies that GB angle only weakly affected the quality of passivation (Figure S9, Supporting Information).

2.3. CO_2 Methanation Activity with Different Applied Potentials and Scans

The catalytic activities after selective electrochemical dissolution are compared in **Figure 4**a. The *XY*-scan Ni-SCR with a P1 pattern was used for comparison of the activities. Before the selective electrochemical dissolution, the as-printed Ni-SCR, which was mostly covered with a layer of Cr and Fe, exhibited 0.15% CO_2 conversion and 9.8% CH_4 selectivity. Simple chemical treatment in 50 wt% NaOH for 12 h slightly increased the CO_2 conversion to 0.44% and the CH_4 selectivity to 16.6%; however, the conversion remained less than 1%. Notably, after being subjected to selective electrochemical dissolution at 50 $mV_{Hg/HgO}$, the Ni-SCRs showed a drastic increase in conversion and selectivity to 70.2% and 98.5%, respectively. This improvement is attributed to the selective dissolution process transforming the surface into a Ni-rich surface and thereby promoting CO_2 methanation because Ni acts as an active site for adsorbing CO_2 and converting it into CH_4. CO_2 temperature-programmed desorption (CO_2-TPD) profiles for the as-printed Ni-SCR do not show any peak, whereas the profiles for the specimens after selective electrochemical dissolution at 50 $mV_{Hg/HgO}$ show CO_2 desorption peaks in the temperature range 250–450 °C because they possess adsorption sites that play a more important role in the CO_2 methanation process (Figure S10, Supporting Information).[39] In addition, the CO_2 methanation activity under an applied potential varied proportionally with the Ni content measured by EDS and XPS (Figure 2b and Figure S4, Supporting Information), revealing that the highest Ni content was achieved under an applied potential of 50 $mV_{Hg/HgO}$, accelerating the CO_2 methanation.

The difference in selective dissolution between the *X*- and *XY*-scan Ni-SCRs led to different catalytic activities toward CO_2 methanation (Figure 4b). Notably, the conversion of CO_2 for the *XY*-scan Ni-SCR was ≈1.3 times greater than that for the *X*-scan Ni-SCR at both 250 and 300 °C. This result suggests that the thicker $Ni(OH)_2$ layer on the *XY*-scan Ni-SCR promoted CO_2 methanation because this Ni-SCR contained more Ni active sites than the *X*-scan Ni-SCR. This difference is evidenced by the CO_2-TPD profiles, where the profile for the *XY*-scan Ni-SCR exhibits slightly stronger desorption peaks than the profile for the *X*-scan Ni-SCR for intermediate basic sites (Figure S10, Supporting Information).

Another important factor governing the catalytic activity of the Ni-SCRs is their geometric structure. Different geometric structures result in different hydrodynamic properties, which in turn result in different catalytic activities.[40] Hence, the Ni-SCRs with four different patterns (P1, P2, P3, and P4) were investigated after the selective electrochemical dissolution process at 50 $mV_{Hg/HgO}$. The outer parts of all the patterned Ni-SCRs, as well as interior of the pore structure, were uniformly transformed from gray to dark-green after selective electrochemical dissolution (Figure 4c and Figure S11, Supporting Information). The conversion started at 200 °C and gradually increased with increasing pattern density (Figure 4d). Interestingly, a sharp increase in conversion between 200 and 250 °C was observed for the P3 and P4 SCRs, whereas the P1 and P2 specimens exhibited low conversion rates (≈10%). In the range 250–400 °C, whereas the conversion rates for the P1 and P2 SCRs increased continuously with increasing temperature, those of the P3 and P4 SCRs reached a maximum and then started to decrease beyond 400 °C. The maximum CO_2 conversion rate of 80.9%, which is close to thermodynamic equilibrium, was achieved for the P4 SCR at 350 °C.

The effect of the flow rate on the reliability of the Ni-SCRs was investigated because decreasing CO_2 conversion rate with increasing flow rate is a known problem.[14] The increase in flow rate results in a decrease in residence time, consequently causing the reactants to pass through the reactor without undergoing any significant reaction.[41] This effect is particularly prominent in monolith reactors, which exhibit low-pressure drops with the laminar flow within their large straight channels.[42–44] As shown in Figure 4e, the CO_2 conversion rate and CH_4 selectivity at a flow

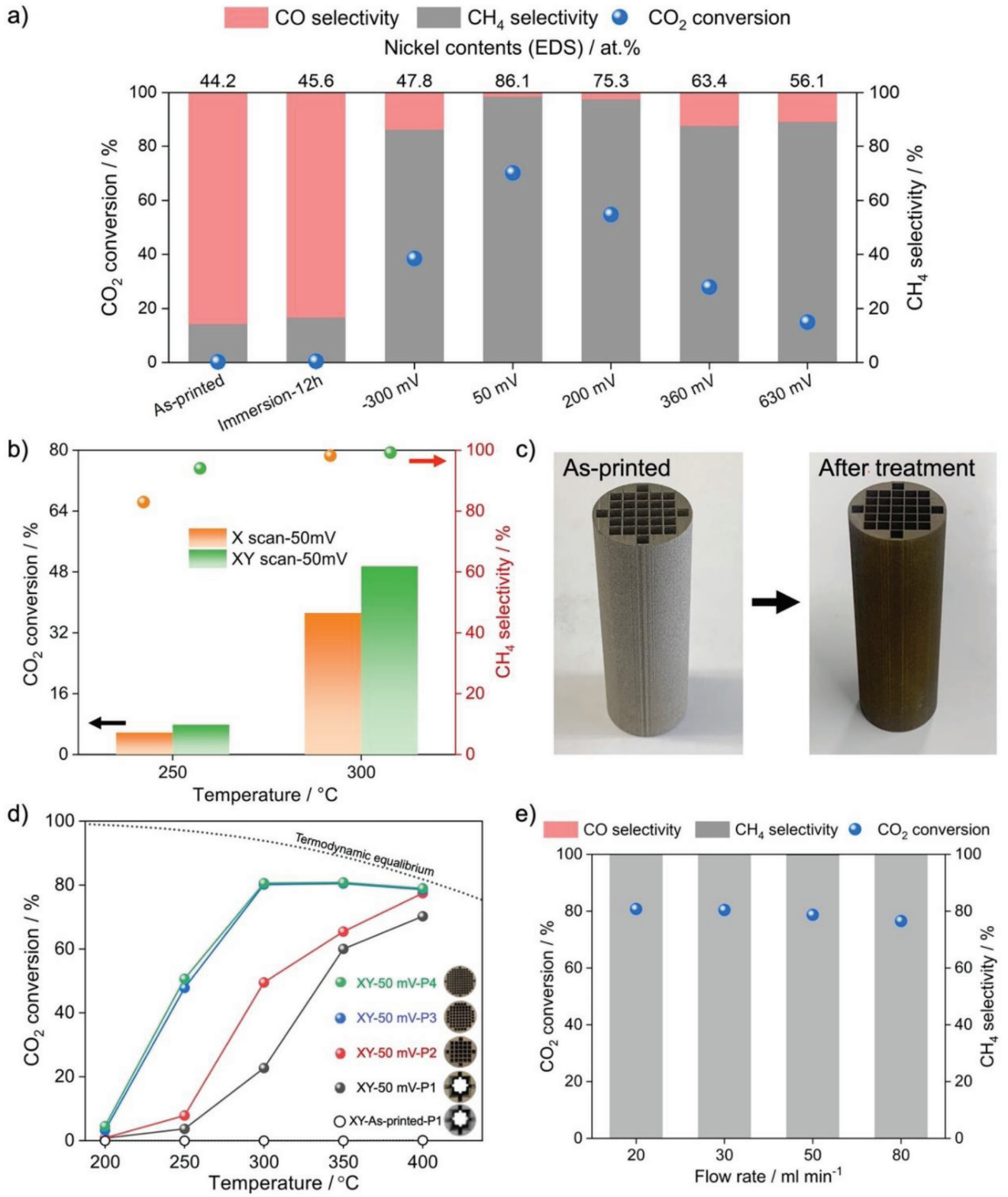

Figure 4. a) CO_2 conversion and product selectivity for SCR-P1 under different applied potentials. b) CO_2 conversion and product selectivity with *X*- and *XY*-scan SCR-P1 specimens under applied potential of 50 $mV_{Hg/HgO}$. c) Photographs of as-printed and treated SCRs subjected to applied potential of 50 $mV_{Hg/HgO}$. d) CO_2 conversion for as-printed SCR and SCRs with four different patterns under applied potential of 50 $mV_{Hg/HgO}$. e) CO_2 conversion and product selectivity for different flow rates. Reaction conditions: $P = 0.1$ MPa; $H_2/CO_2/N_2 = 64/16/20$; flow rate = 20 mL min^{-1} in (a), (b), and (d) and 20–80 mL min^{-1} in (e).

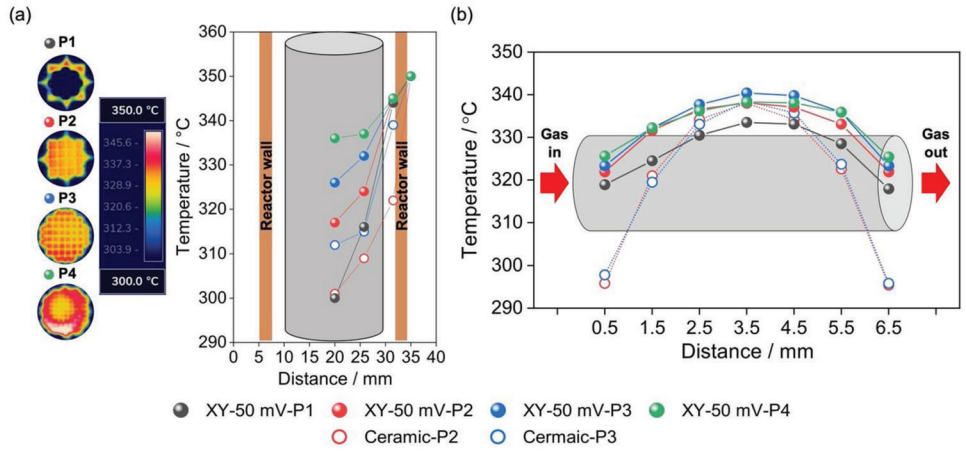

Figure 5. a) Infrared camera images and radial temperature profiles for SCR and Ni-impregnated ceramic reactor with different patterns under air-exposure conditions (ex situ). b) Axial temperature profiles for SCR and Ni-impregnated ceramic reactor with different patterns under CO_2 methanation conditions (in situ). Reaction conditions: $P = 0.1$ MPa; $H_2/CO_2/N_2 = 64/16/20$; flow rate = 80 mL min^{-1}.

rate of 20 mL min^{-1} were 80.9% and greater than 99.8%, respectively. With increasing flow rate, the conversion rate decreased slightly but remained greater than 76.2% even at 80 mL min^{-1} and the CH_4 selectivity remained greater than 99.8%.

To gain a deeper insight into the relationship between geometric structure and activity, the thermal properties of the SCR should be considered because the catalytic performance drastically varies with the temperature distribution in the reactor.[44] **Figure 5**a shows infrared thermal images and a radial temperature profile at 350 °C in the air-exposed reactor. Detailed measurement points are described in Figure S12, Supporting Information. The increase in pattern density from P1 to P4 promoted a uniform thermal distribution over the whole SCR as well as a decrease in the radial temperature drop between the exterior and interior of the SCR. These effects were attributed to the high thermal conductivity through the compactly connected thin channel as a result of the increase in pattern density (Table S5, Supporting Information).[45] In addition, compared with a Ni-impregnated ceramic reactor, the Ni-SCRs clearly showed a smaller radial temperature decrease because of the higher thermal conductivity for the Ni-SCRs than that for the ceramic reactor. Furthermore, the in situ axial temperature profiles under CO_2 methanation conditions indicate that a uniform temperature distribution in the axial direction was achieved in the SCRs as the pattern density increased from P1 to P4, whereas the formation of a hotspot was identified at 3.5 mm in the ceramic reactor. These results indicate that the high thermal conductivity prevented hotspot formation in the axial direction and distributed the thermal energy over the entire reactor with increasing pattern density. Therefore, because of the prevention of hotspots and the uniform temperature profiles in the P4 SCR, this reactor showed the optimal activity toward CO_2 methanation among the investigated reactors.

2.4. Refreshment of Ni-SCR

In general, catalysts for the methanation of CO_2 are deactivated by sintering and carbon deposition, and the deactivated catalysts are conventionally regenerated via H_2 reduction at high temperatures.[46] Unfortunately, most of the previously reported catalysts suffer from irreversible deactivation and must be replaced or recycled via complex processes.[47] By contrast, the active sites of the Ni-SCRs were generated from the SCRs themselves rather than from an externally supplied material, suggesting that the active sites on the Ni-SCRs can be restored through self-dissolution upon application of an appropriate treatment.

Figure 6a shows the results of long-term stability tests with the *XY*–50 mV–P4 Ni-SCR, including the refresh process. After the first 72 h of reaction, the SCR maintained high CO_2 conversion and CH_4 selectivity rates greater than 73.8% and 99.8%, respectively. By contrast, the Ni-impregnated ceramic reactor was deactivated more rapidly than the SCR, similar to the behavior of typical Ni catalysts (Figure S13, Supporting Information).[48] In the case of the P4-SCR, the high thermal conductivity prevented sintering and contributed to the SCR's high stability, whereas the ceramic reactor with low thermal conductivity was sintered by hotspots. Nevertheless, even though the SCR showed high stability for 72 h, the CO_2 conversion process was irreversibly deactivated by sintering and could not be recovered by the conventional H_2 reduction process (Table S6, Supporting Information).

To address the deactivation problem, we conducted a simple chemical treatment using 50 wt% NaOH, which was the same solution used in the selective electrochemical dissolution process, as a refresh process to regenerate active sites on the SCR. After such a straightforward treatment, the CO_2 conversion and CH_4 selectivity rates recovered from 74.8% to 81.1% and from 99.82% to 99.96%, respectively. More interestingly, the recovered catalytic performance was substantially better than the initial one. In addition, XPS analysis showed that the near-surface Ni content of the used SCR increased from 59.3 at% to 73.5 at% as $Ni(OH)_2$ or γ-NiOOH species after the refresh treatment (Figure 6b and Figure S14, Supporting Information). SEM and XRD results show that the surface morphology of the SCR after the reaction for 72 h was a Ni layer containing crack or void regions formed by the contraction of the initial $Ni(OH)_2$ layer during the reduction and catalytic reaction (Figure 6c and Figures S15 and S16, Supporting Information). However, after a refresh process, the crack- or void-containing regions were fully covered

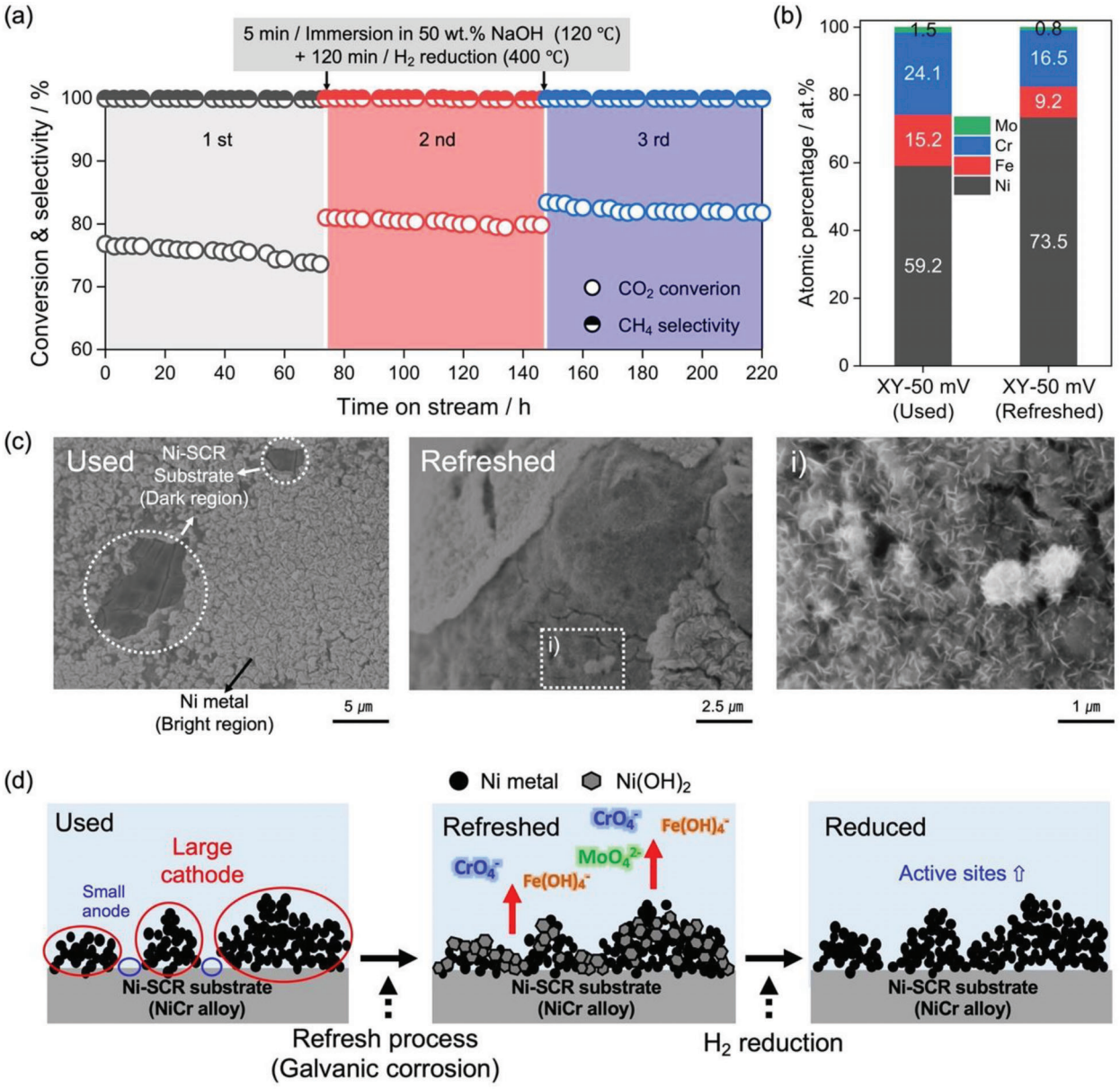

Figure 6. a) Long-term stability test of *XY*–50 mV–P4 SCR with multiple refresh processes. b) Surface elemental composition of used and refreshed SCR measured by XPS. c) Surface morphology variation before and after refresh process. d) Schematic of mechanism for self-dissolution refresh process.

by precipitated $Ni(OH)_2$. When the used SCR was immersed in a 50 wt% NaOH solution as a refresh process, the exposed Ni-SCR substrate containing Cr and Fe acted as an anode, whereas the Ni moiety served as a cathode, promoting galvanic corrosion due to the difference in the standard electrode potentials of Cr, Fe, and Ni (−0.838, −0.538, and −0.338 $mV_{Hg/HgO}$ at 25 °C, respectively), as illustrated in Figure 6d.[49] In general, the most active Cr species in Ni alloys rapidly form a compact few-nanometer Cr oxide layer in an acidic or neutral environment, preventing further galvanic corrosion.[50] However, in a hot alkaline solution, the Cr oxide layer is highly unstable and is easily transformed into CrO_4^{2-} because of the reducing environment, which accelerates the selective dissolution of Cr and Fe ions from the remaining exposed Ni alloy substrate by galvanic corrosion.[24]

To comprehensively investigate the galvanic corrosion between Ni and Ni-SCRs, we conducted a zero-resistance ammeter test to demonstrate that the amount of exposed Ni on the Ni-SCR substrates accelerates galvanic corrosion via small anode–large cathode coupling, in which the high overpotential was applied to the small anode (Figure S17, Supporting Information). The variation of the surface area ratio between pure Ni and the Ni-SCR substrate from 1 to 10 resulted in a proportional increase in the galvanic corrosion density from 10.4 to 48.2 μA cm^{-1} (Figure S18, Supporting Information). Without Ni enrichment on the SCR

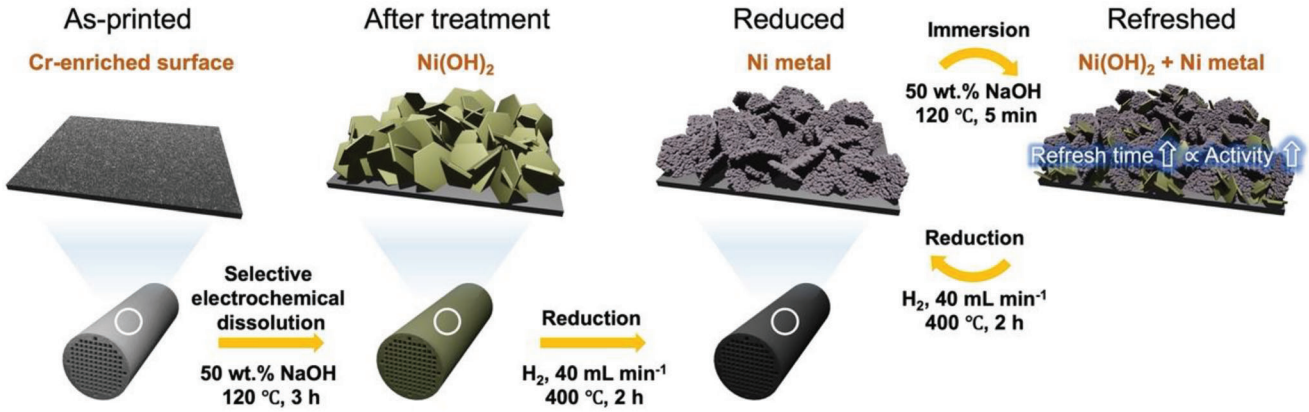

Figure 7. Schematic of fabrication and refresh processes for metal 3D-printed SCRs for CO_2 methanation.

surface by the selective electrochemical dissolution process, no active refresh process occurred in the Ni-SCR because the driving force for galvanic corrosion was insufficient when the concentration of Ni on the surface region was low and the parting limit for dealloying was not satisfied, which led to no activity toward CO_2 methanation even after immersion Ni-SCR in 50 wt% NaOH solution for 12 h (Figure 4a).[24] Consequently, the refresh process for used Ni-SCR facilitated the selective dissolution of Cr, Fe, and Mo to expose fresh $Ni(OH)_2$ within a short time (Table S7, Supporting Information). Similarly, a third long-term stability test after the second refresh process also showed overperformance compared with the second reaction, including an 83.4% CO_2 conversion rate and a 99.9% CH_4 selectivity; these results indicate that the CO_2 methanation activity continuously increased with increasing number of refresh processes and that the stability remained high (average 1.48% reduction in CO_2 conversion rate).

In summary, all of the investigated fabrication processes for a robust SCR for CO_2 methanation are illustrated in **Figure 7**. Before the selective electrochemical dissolution process, the as-printed SCR surface, which consisted of a Cr-enriched surface, is inactive toward CO_2 methanation. However, with the simple selective electrochemical dissolution of Cr, Fe, and Mo components at 50 $mV_{Hg/HgO}$ in 50 wt% NaOH solution for 3 h, the surface of the Ni-SCR became $Ni(OH)_2$-enriched. The *XY*-scan Ni-SCR surface, whose microstructure consisted of coarse grains with few dislocations, formed more $Ni(OH)_2$ than the *X*-scan Ni-SCR surface. After H_2 reduction, the Ni-SCR exhibited high activity and reliable stability toward CO_2 methanation. Moreover, the simple refresh process based on the self-dissolution mechanism regenerated active Ni sites, which continuously increased the catalytic activity during the refresh process, resulting in an SCR that showed overperformance compared with its initial activity.

3. Experimental Section

Preparation of SCR: Hastelloy X powder (EOS, Krailling, Germany) prepared by a gas-atomization process was used as a starting material. The chemical composition and SEM images are shown in Table S1 and Figure S1, Supporting Information, respectively. EOS M 290 (EOS, Krailling, Germany) was used for LPBD, and a cylinder-shaped SCR 23 mm in diameter and 70 mm long and with four different cell densities (P1, P2, P3, and P4) was fabricated using two different scan strategies: *X* and *XY* scans. The building platform was heated to 80 °C, and the O_2 concentration was maintained at less than 100 ppm by Ar gas flow. The laser power *P* was 250 W, the scan speed *v* was 1000 mm, the hatch distance *d* was 0.1, and the layer thickness *t* was 0.06 mm. A thin substrate with dimensions of 10 mm × 20 mm × 0.5 mm was also fabricated using a similar method for detailed characterization of the specimens.

Selective Electrochemical Dissolution Process: A 50 wt% NaOH electrolyte solution (500 g) was added to a 500 mL Teflon beaker. The SCR was positioned in the center of the Teflon beaker, and a working electrode and three Pt counter electrodes were placed around the SCR with even distance to form a uniform electrical field. A Hg/HgO electrode ($HgO + H_2O + 2e^- \rightleftharpoons Hg + 2OH^-$, $E_0 = 0.098$ V vs normal hydrogen electrode at 25 °C) was used as standard electrode and was filled with 7 M NaOH to minimize the potential drop by a liquid junction. Five different potentials were applied using a HZ-7000 electrochemical measurement system (Hokuto Denko, Tokyo, Japan). After the electrochemical treatment, the SCR was washed five times with deionized water and dried in an 80 °C oven for 2 h. For comparison, a simple Ni-impregnation method was used to impregnate Ni into a cordierite monolithic reactor ($2MgO{\cdot}2Al_2O_3{\cdot}5SiO_2$) with P2 and P3 patterns (Iwao Jiki Kogyo, Aritacho, Japan). The impregnation method was the same as that in ref. [51].

Evaluation of CO_2 Methanation Activity: The CO_2 methanation performance was evaluated using a fixed-bed reactor system in which an SCR was placed in a quartz cell held within a ribbon heater. All of the SCRs were pretreated with H_2 gas (40 mL min^{-1}) at 400 °C for 2 h. The H_2-pretreated SCR was subsequently cooled to the desired reaction temperature, and the methanation of CO_2 was carried out with a mixed feed gas ($H_2/CO_2/N_2 = 64:16:20$) at a flow rate of 20–80 mL min^{-1}. The gas products were analyzed using an online gas chromatograph (Shimadzu GC-14B) equipped with an active carbon column connected to a flame ionization detector combined with a methanizer. The conversion and selectivity were calculated as follows:

$$CO_{2_{conversion}}(\%) = \frac{CO_{2_{in}} - CO_{2_{out}}}{CO_{2_{in}}} \times 100\% \quad (1)$$

$$CH_{4_{selectivity}}(\%) = \frac{CH_{4_{out}}}{CO_{2_{in}} - CO_{2_{out}}} \times 100\% \quad (2)$$

Supporting Information

Supporting Information is available from the Wiley Online Library or from the author.

Acknowledgements

This work was supported by Grants-in-Aid for Scientific Research (A21H050980 and T22K189200) from the Japan Society for the Promotion of Science (JSPS). This work was also partly supported by the Cross-Ministerial Strategic Innovation Promotion Program (SIP), Materials Integration for Revolutionary Design System of Structural Materials, Domain C1: "Development of Additive Manufacturing Process for Ni-based Alloy" from the Japan Science and Technology Agency (JST).

Conflict of Interest

The authors declare no conflict of interest.

Data Availability Statement

The data that support the findings of this study are available from the corresponding author upon reasonable request.

Keywords

catalysts, CO_2 methanation, electrochemical selective dissolution, metal 3D printing, selective laser melting, self-catalytic reactors

Received: April 11, 2023
Revised: May 12, 2023
Published online:

[1] C. Vogt, M. Monai, G. J. Kramer, B. M. Weckhuysen, *Nat. Catal.* **2019**, *2*, 188.
[2] L. Shen, J. Xu, M. Zhu, Y. F. Han, *ACS Catal.* **2020**, *10*, 14581.
[3] Z. Zhang, Y. Zheng, L. Qian, D. Luo, H. Dou, G. Wen, A. Yu, Z. Chen, *Adv. Mater.* **2022**, *34*, 2201547.
[4] W. C. Chueh, C. Falter, M. Abbott, D. Scipio, P. Furler, S. M. Haile, S. Aldo, *Science* **2010**, *330*, 1797.
[5] K. Mori, N. Hashimoto, N. Kamiuchi, H. Yoshida, H. Kobayashi, H. Yamashita, *Nat. Commun.* **2021**, *12*, 3884.
[6] R. P. Ye, J. Ding, W. Gong, M. D. Argyle, Q. Zhong, Y. Wang, C. K. Russell, Z. Xu, A. G. Russell, Q. Li, M. Fan, Y. G. Yao, *Nat. Commun.* **2019**, *10*, 5698.
[7] T. Cui, L. Li, C. Ye, X. Li, C. Liu, S. Zhu, W. Chen, D. Wang, *Adv. Funct. Mater.* **2022**, *32*, 2108381.
[8] S. Gao, S. Hao, Z. Huang, Y. Yuan, S. Han, L. Lei, X. Zhang, R. Shahbazian-Yassar, J. Lu, *Nat. Commun.* **2020**, *11*, 2016.
[9] J. T. Richardson, *Principles of Catalyst Development*, Springer, New York **2013**.
[10] J. R. H. Ross, *Heterogeneous Catalysis: Fundamentals and Applications*, Elsevier, New York **2011**.
[11] C. G. Hill, T. W. Root, *Introduction to Chemical Engineering Kinetics and Reactor Design*, John Wiley & Sons, New York **2014**.
[12] Q. Wei, H. Li, G. Liu, Y. He, Y. Wang, Y. E. Tan, D. Wang, X. Peng, G. Yang, N. Tsubaki, *Nat. Commun.* **2020**, *11*, 4098.
[13] A. Ambrosi, M. Pumera, *Adv. Funct. Mater.* **2018**, *28*, 1700655.
[14] C. Wang, X. Peng, Y. He, J. Fan, X. Lin, L. Jiang, N. Tsubaki, *ChemCatChem* **2022**, *14*, 202101581.
[15] Q. Wei, H. Li, G. Liu, Y. He, Y. Wang, Y. E. Tan, D. Wang, X. Peng, G. Yang, N. Tsubaki, *Nat. Commun.* **2020**, *11*, 4098.
[16] G. Groppi, E. Tronconi, *Catal. Today* **2005**, *105*, 297.
[17] S. Lawson, X. Li, H. Thakkar, A. A. Rownaghi, F. Rezaei, *Chem. Rev.* **2021**, *121*, 6246.
[18] A. Vita, C. Italiano, L. Pino, P. Frontera, M. Ferraro, V. Antonucci, *Appl. Catal., B* **2018**, *226*, 384.
[19] B. Mutz, M. Belimov, W. Wang, P. Sprenger, M. A. Serrer, D. Wang, P. Pfeifer, W. Kleist, J. D. Grunwaldt, *ACS Catal.* **2017**, *7*, 6802.
[20] C. Wang, X. Peng, Y. He, J. Fan, X. Lin, L. Jiang, N. Tsubaki, *ChemCatChem* **2022**, *14*, 202101581.
[21] H. Schäfer, S. Sadaf, L. Walder, K. Kuepper, S. Dinklage, J. Wollschläger, L. Schneider, M. Steinhart, J. Hardege, D. Daum, *Energy Environ. Sci.* **2015**, *8*, 2685.
[22] K. Hashimoto, K. Asami, *Corros. Sci.* **1979**, *19*, 427.
[23] A. G. Oshchepkov, G. Braesch, A. Bonnefont, E. R. Savinova, M. Chatenet, *ACS Catal.* **2020**, *10*, 7043.
[24] T. Ghaznavi, M. A. Bryk, S. Y. Persaud, R. C. Newman, *Corros. Sci.* **2022**, *197*, 110003.
[25] R. B. Rebak, *NACE – Int. Corros. Conf. Ser.* **2006**, *2006*, 065011.
[26] H. Gholamzadeh, B. Alsekhan, A. Shaik, K. Daub, S. Y. Persaud, *J. Electrochem. Soc.* **2022**, *169*, 081508.
[27] D. Macdonald, *ECS Meet. Abstr.* **2006**, *MA2006-01*, 318.
[28] B. P. Payne, M. C. Biesinger, N. S. McIntyre, *J. Electron Spectrosc. Relat. Phenom.* **2009**, *175*, 55.
[29] J. Akram, P. Chalavadi, D. Pal, B. Stucker, *Addit. Manuf.* **2018**, *21*, 255.
[30] S. H. Sun, K. Hagihara, T. Nakano, *Mater. Des.* **2018**, *140*, 307.
[31] Y. Yin, H. Li, S. Pan, J. Zhang, Q. Han, S. Yang, *Corros. Sci.* **2022**, *206*, 110494.
[32] C. Escrivà-Cerdán, E. Blasco-Tamarit, D. M. García-García, J. García-Antón, R. Akid, J. Walton, *Electrochim. Acta* **2013**, *111*, 552.
[33] L. Liu, Y. Li, F. Wang, *Electrochim. Acta* **2007**, *52*, 7193.
[34] T. Ishimoto, K. Hagihara, K. Hisamoto, T. Nakano, *Addit. Manuf.* **2021**, *43*, 102004.
[35] C. Y. Liu, J. D. Tong, M. G. Jiang, Z. W. Chen, G. Xu, H. B. Liao, P. Wang, X. Y. Wang, M. Xu, C. S. Lao, *Mater. Sci. Eng., A* **2019**, *766*, 138364.
[36] H. Y. Wan, Z. J. Zhou, C. P. Li, G. F. Chen, G. P. Zhang, *Mater. Sci. Eng., A* **2019**, *753*, 42.
[37] K. D. Ralston, N. Birbilis, *Corrosion* **2010**, *56*, 1729.
[38] Y. Yin, J. Zhang, S. Yang, T. Liu, Q. Han, Z. Zhang, H. Yang, *Mater. Des.* **2021**, *206*, 109828.
[39] Y. Chen, B. Qiu, Y. Liu, Y. Zhang, *Appl. Catal., B* **2020**, *269*, 118801.
[40] A. Quintanilla, G. Vega, P. Lopez, F. Garcia, E. Madurga, M. Belmonte, J. A. Casas, *Ind. Eng. Chem. Res.* **2021**, *60*, 14701.
[41] E. B. Nauman, *Chemical Reactor Design, Optimization, and Scaleup*, 2nd ed., Wiley, New York **2007**.
[42] Z. Jiang, K. S. Chung, G. R. Kim, J. S. Chung, *Chem. Eng. Sci.* **2003**, *58*, 1103.
[43] K. G. Manoharan, V. V. Buwa, *Ind. Eng. Chem. Res.* **2019**, *58*, 22363.
[44] H. L. Huynh, W. M. Tucho, Q. Shen, Z. Yu, *Chem. Eng. J.* **2021**, *428*, 131106.
[45] C. G. Visconti, G. Groppi, E. Tronconi, *Chem. Eng. J.* **2013**, *223*, 224.
[46] D. Schmider, L. Maier, O. Deutschmann, *Ind. Eng. Chem. Res.* **2021**, *60*, 5792.
[47] N. M. Al-Mansi, N. M. A. Monem, *Waste Manage.* **2002**, *22*, 85.
[48] Y. Chen, B. Qiu, Y. Liu, Y. Zhang, *Appl. Catal., B* **2020**, *269*, 118801.
[49] V. M. Schmidt, *Elektrochemische Verfahrenstechnik: Grundlagen, Reaktionstechnik, Prozessoptimierung*, John Wiley & Sons, New York **2012**.
[50] X. Li, J. D. Henderson, F. P. Filice, D. Zagidulin, M. C. Biesinger, F. Sun, B. Qian, D. W. Shoesmith, J. J. Noël, K. Ogle, *Corros. Sci.* **2020**, *176*, 109015.
[51] Q. Huang, Z. Y. Zhang, W. J. Ma, Y. W. Chen, S. M. Zhu, S. B. Shen, *J. Ind. Eng. Chem.* **2012**, *18*, 757.